

Nanoscale spatial organization of the *HoxD* gene cluster in distinct transcriptional states

Pierre J. Fabre^a, Alexander Benke^b, Elisabeth Joye^a, Thi Hanh Nguyen Huynh^c, Suliana Manley^{b,1}, and Denis Duboule^{a,c,1}

^aSchool of Life Sciences, Ecole Polytechnique Fédérale de Lausanne, 1015 Lausanne, Switzerland; ^bLaboratory of Experimental Biophysics, Ecole Polytechnique Fédérale de Lausanne, 1015 Lausanne, Switzerland; and ^cDepartment of Genetics and Evolution, University of Geneva, 1211 Geneva 4, Switzerland

Contributed by Denis Duboule, September 14, 2015 (sent for review July 21, 2015; reviewed by Victor Corces and Luca Giorgetti)

Chromatin condensation plays an important role in the regulation of gene expression. Recently, it was shown that the transcriptional activation of *HoxD* genes during vertebrate digit development involves modifications in 3D interactions within and around the *HoxD* gene cluster. This reorganization follows a global transition from one set of regulatory contacts to another, between two topologically associating domains (TADs) located on either side of the *HoxD* locus. Here, we use 3D DNA FISH to assess the spatial organization of chromatin at and around the *HoxD* gene cluster and report that although the two TADs are tightly associated, they appear as spatially distinct units. We measured the relative position of genes within the cluster and found that they segregate over long distances, suggesting that a physical elongation of the *HoxD* cluster can occur. We analyzed this possibility by super-resolution imaging (STORM) and found that tissues with distinct transcriptional activity exhibit differing degrees of elongation. We also observed that the morphological change of the *HoxD* cluster in developing digits is associated with its position at the boundary between the two TADs. Such variations in the fine-scale architecture of the gene cluster suggest causal links among its spatial configuration, transcriptional activation, and the flanking chromatin context.

DNA FISH | super-resolution microscopy | limb development | topologically associating domains | *HoxD*

In the nuclei of mammalian cells, chromatin is packaged according to several levels of organization (1–3), which can either reflect or affect transcriptional regulation (e.g., ref. 4). By combining DNA FISH and microscopy, it was shown that chromatin decondensation occurs concomitantly with transcriptional activation (5), suggesting that the opening of chromatin makes gene promoters accessible for transcription. Recently, however, studies involving super-resolution microscopy have revealed a more complex relationship, showing that a higher compaction of chromatin can also be associated with an active state of transcription (6). In this latter case, the compaction of local regulatory elements allowed for a stronger enhancer effect, leading to a more robust activation.

Approaches based on chromosome conformation capture [and derivatives thereof (7)] at the mammalian *HoxD* locus have revealed that interactions between genes and their enhancers can occur not only during an active phase of transcription but also in the absence of transcriptional read out, in cells that do not necessarily express the related target genes (8). Such constitutive contacts covering large regulatory landscapes and their target gene or genes were found to be present in mammals genome-wide (9) and are referred to as topologically associating domains, or TADs (9, 10). TADs have been associated with a variety of regulatory functions (11), either in their implementation (e.g., ref. 12) or in their emergence during vertebrate evolution (13, 14).

Hox gene clusters have been successfully used to study the functional organization of TADs (15–17), as well as the relationship between the progressive decompaction of both genes and enhancers and their transcriptional read-out. Studies of the mouse *HoxD* cluster have provided insights into the global regulation of its nine consecutive genes during limb development, including the presence of multiple regulatory sequences spanning a

2-megabase large DNA interval (18). Recently, this gene cluster, similar to its *HoxA* relative (14, 15), was shown to reside at a boundary between two TADs (located ca. between *Hoxd11* and *Hoxd12*), with each TAD containing enhancers required to regulate different subgroups of genes in developing organs or structures (9, 16, 19) such as distal limbs, proximal limbs, genitals, or the cecum. Interestingly, all enhancers sharing a particular specificity are found within the same TAD, and thus far, no cell type or tissue was reported where these two opposite regulatory landscapes would operate concomitantly (8, 16, 17, 19), suggesting a functional switch occurs between these two TADs in their capacity to regulate subsets of target *Hoxd* genes.

TADs were originally defined by biochemical approaches (9, 10). The correspondence between the averaging of multiple interactions, some of them of unknown significance, on the one hand (see ref. 20), and a chromatin structure in the nuclear space of single cells, on the other hand, is of great interest and has recently come under discussion (see ref. 21). In this study, we used DNA FISH to show that the two TADs splitting the *HoxD* locus are distinct chromatin units, which rarely overlap despite their close association in space. Within this well-defined 3D organization, *Hoxd* genes can segregate over large distances. By using super-resolution microscopy, we observe that these large distances result from extensive elongation events over relatively short genomic distances, which appear to be maximal in tissue with high levels of *Hoxd* gene transcription. Our data suggest this elongation of the *HoxD* cluster is facilitated by its genomic position at the boundary between two TADs.

Significance

Ultrastructural chromatin dynamics may play a key role in regulating transcriptional activation. Here we have used super-resolution microscopy to study the folding mechanics of the *HoxD* cluster, as assayed by following the elongation of chromatin in single cells with different status of *Hox* gene activation. We observed that the spatial separation of *Hoxd* genes is strongest in those tissues where they are highly expressed. We also document that the opening of chromatin precedes transcription and that the strongest elongations are observed at the location of the boundary between two major topologically associating domains (TADs). These results shed light on how spatial compartmentalization is achieved, likely to accompany efficient chromatin reorganization upon activation of transcriptional switches.

Author contributions: P.J.F., S.M., and D.D. designed research; P.J.F., A.B., E.J., and T.H.N.H. performed research; S.M. and D.D. contributed new reagents/analytic tools; P.J.F., A.B., E.J., and S.M. analyzed data; and P.J.F., A.B., S.M., and D.D. wrote the paper.

Reviewers: V.C., Emory University; and L.G., Friedrich Miescher Institute for Biomedical Research.

The authors declare no conflict of interest.

Freely available online through the PNAS open access option.

Data deposition: The RNA-seq data reported in this paper have been deposited in the Gene Expression Omnibus (GEO) database, www.ncbi.nlm.nih.gov/geo (accession no. [GSE72285](#)).

¹To whom correspondence may be addressed. Email: Denis.Duboule@epfl.ch or suliana.manley@epfl.ch.

This article contains supporting information online at www.pnas.org/lookup/suppl/doi:10.1073/pnas.1517972112/-DCSupplemental.

Results

Hoxd Genes Are Localized at the Boundary Between Two TADs. To directly observe the chromatin topology surrounding the *HoxD* cluster, we used 3D DNA FISH by labeling several consecutive BACs per TAD, such as to cover each TAD with a different color (Fig. 1*A* and *SI Appendix, Table S1*), and thus to assess the general chromatin spatial organization surrounding *HoxD* (Fig. 1*B*). In both active (forelimb) and inactive (forebrain) cells, we observed that TADs are organized as two dense and distinct units, closely associated in the nuclear space (Fig. 1*C*). High-resolution images using structured illumination microscopy showed that the TADs did not intermingle, and rarely overlapped in any substantial manner (Fig. 1*D*). This segregation was much less pronounced when BAC probes belonging to the same TAD were used as controls (*SI Appendix, Fig. S1*).

We measured the distance between TAD centers, which ranged from 0.20 to 1.40 μm , with an average of about 0.79 μm ($n > 1,000$ pairs). Because previous studies using chromosome conformation capture (4C) had revealed a dynamic switch in contacts between *Hoxd* genes and the two TADs in the proximal versus distal parts of developing forelimbs (16), we assessed whether this inter-TAD distance would change between these distinct limb domains, but found no significant difference (Fig. 1*B*, *C*, and *E*). A detailed analysis of chromatin morphology revealed that the TADs are rather compact, with low ellipticity (Fig. 1*F*). We nevertheless observed a slight variation in ellipticity in cellular domains displaying different *Hoxd* gene expression patterns. Both TADs indeed appeared slightly less elongated in presumptive digit cells in the distal part of the limb (Fig. 1*F*), yet their global structure was rather stable in all analyzed situations. Finally, we assessed the position of the *HoxD* cluster relative to the TADs, using a 39-kb large fosmid probe covering the *Hoxd8* to *Hoxd12* genes. As expected, the signal was consistently detected at the interface between the two chromatin domains (Fig. 1*G*). In some cases, the *HoxD* cluster signal appeared somewhat elongated (arrowheads, Fig. 1*G*).

Hoxd Genes Are Close to Their Regulatory Islands. The fact that TADs display comparably condensed aspects in both proximal and distal limb cells *in vivo*, that is, independent from their transcriptional activities, supports the view of a preformed or poised “background regulatory structure” (8); that is, a state of preferential chromatin compaction within a given TAD in which constitutive interactions occur without necessarily eliciting a transcriptional output (9, 11). In a previous study using FISH in ES cells, the *Hoxd1* gene localized at a substantial distance from *Hoxd13*, suggesting that the *HoxD* cluster could display spatially distinct moieties with its centromeric region (containing *Hoxd13*) positioned at the TAD boundary (22). To assess whether this apparent decompaction of *Hoxd* genes is linked to their relative topological position within the cluster and, consequently, whether their inclusion into either one of the TADs or their location at the inter-TADs boundary could explain this tendency to decompact, we examined the spatial relationships between four different parts of the *HoxD* cluster.

We used fosmid clones either covering the *Hoxd1* gene or the *Hoxd3* to *Hoxd4* region, (i.e., two regions normally included within the telomeric TAD), covering the *Hoxd13* gene, and hence entirely positioned within the centromeric TAD, or covering the *Hoxd8* to *Hoxd12* region located at or around the inter-TAD boundary (16) (Fig. 1*H*). We measured the distances between combinations of two probes and found that parts of the *HoxD* cluster could be separated from one another by more than 500 nm (Fig. 1*I–K*). Of note, the distances measured between the centers of both signals generally correlate with the genomic distance (Fig. 1*J* and *SI Appendix, Table S2*). In this respect, we noticed that the telomeric extremity of the *HoxD* cluster, as monitored by the *Hoxd1* probe, was clearly separated from the main part of the cluster, with an average distance between *Hoxd1* and *Hoxd11* or *Hoxd13* of more than 700 nm (Fig. 1*J*). This apparent separation

between *Hoxd1* and the rest of the cluster was, however, not constant and followed a broad distribution (Fig. 1*K*).

Super-Resolution Microscopy of the *HoxD* Locus. This spatial separation between different parts of the *HoxD* cluster is reminiscent of a model in which groups of active and inactive genes within *HoxD* form physically distinct and highly dynamic subdomains (23). To more directly examine the conformation of the *HoxD* cluster in single cells, we labeled its entire genomic sequence by using a 160-kb large BAC as a DNA probe and carried out DNA FISH. The morphology of the *HoxD* cluster was subsequently resolved using stochastic optical reconstruction microscopy (STORM), a type of super-resolution imaging based on sequential imaging of single-molecule signals (24–26). As a control, we used a probe of similar size located nearby, within the telomeric gene desert (Fig. 2*A*).

We initially examined sections of embryonic brain where the *HoxD* cluster is transcriptionally silent. Both the control and *HoxD* probes appeared as compact objects (Fig. 2*B* and *E*). However, cells from the developing distal forelimb; that is, a tissue with robust transcription of at least the *Hoxd13* to *Hoxd9* genes (27) (Fig. 3), displayed a higher diversity of morphologies (Fig. 2*C* and *F*). Although the total area of the object appeared unchanged, the signal detected in many cells of the forelimb tissues was substantially more elongated (*SI Appendix, Fig. S2*). We quantified this variation in elongation by the aspect ratio and the circularity of the objects. The major axis of the cluster divided by its minor axis (aspect ratio) was significantly higher in active forelimb cells than in inactive forebrain cells (Fig. 2*H*), where circularity was also lower (Fig. 2*I*).

As elongation was maximal in limb cells displaying a high level of *Hoxd* transcription, we assessed whether transcription could cause elongation by evaluating the cluster morphology in ES cells, a cell type in which *Hoxd* genes have not yet been activated and are labeled by positive and negative chromatin marks, potentially reflective of a poised transcriptional state (28). In these cells, many alleles showed an elongated aspect, with a circularity index close to that scored in forelimb cells, and thus significantly different from the data obtained in brain cells (Fig. 2*D*, *G*, and *I*). From this observation, we conclude that the elongation observed by using STORM microscopy seems to be an important feature of an “open” *HoxD* cluster, observed either in ES cells where the cluster is poised to be transcribed or in cells where transcription indeed occurs. Finally, we measured the extent of the elongated structure and found that the signals can span more than 500 nm. This high extension rate is consistent with our previous measurements (Fig. 1*J*) and is in the range predicted by mathematical modeling (29).

Chromatin Elongation at Super Resolution. The mechanisms underlying such an elongation process are unclear. Opening and/or relaxation of chromatin may be a consequence of active transcription driven by elongating RNA polymerase II and consequent chromatin remodeling. Alternatively, changes in chromatin morphology could result from states of histone modifications not necessarily associated with different transcriptional activities. For example, in both brain and ES cells, the *HoxD* cluster is covered by polycomb-associated chromatin marks such as H3K27me3, which may participate in its compaction via the recruitment of the PRC1 complex (22, 28, 30). However, the H3K27me3 coverage observed over *HoxD* in ES cells is significantly weaker than in brain cells (23), which may be related to the presence of H3K4me3 marks in the former sample. Accordingly, a poised chromatin state may show a level of decompaction comparable to that of transcriptionally active chromatin.

We investigated this issue by using super-resolution microscopy with four smaller DNA probes spanning different subregions of the *HoxD* cluster (Fig. 1*H*, enlarged in Fig. 3*A*). These subregions displayed differential coverage by polycomb-associated marks in either distal or proximal limb bud cells (16), and thus were used to evaluate a potential link between the elongation

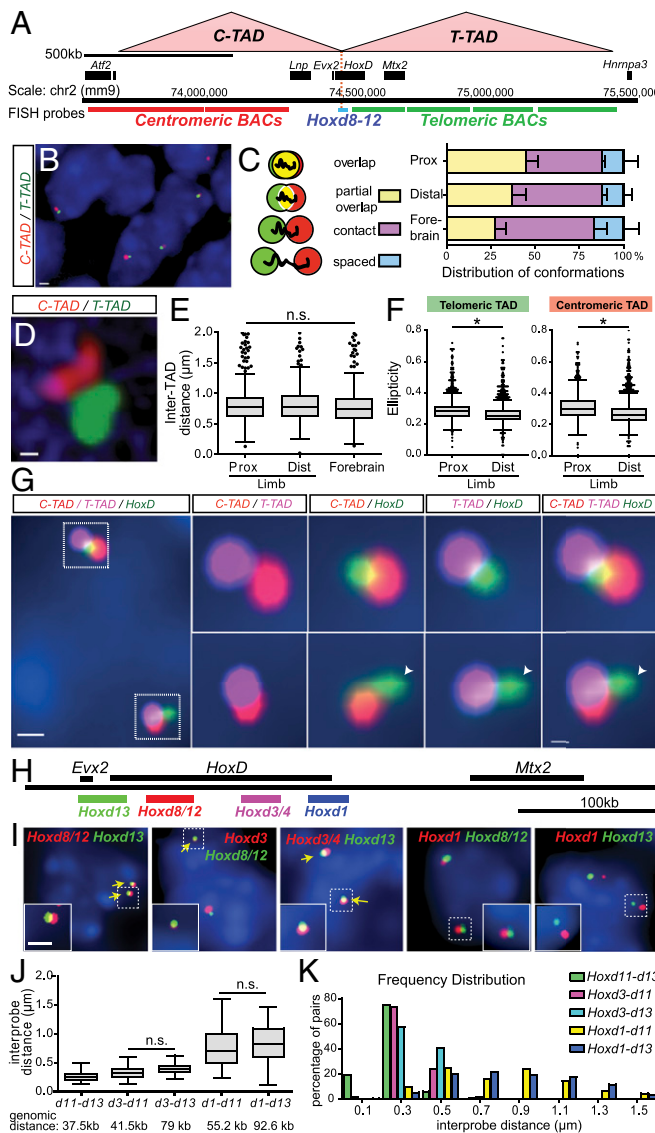


Fig. 1. The *HoxD* cluster is at the interface between two TADs. (A) Schematic of the centromeric and telomeric TADs (C-TAD; T-TAD) using public data available under ref. 9 with genes as black boxes below and the relative localization of the probes (in red, blue and green) used in the DNA FISH experiments. The red dotted line represents the TAD boundary within *HoxD*. (B) E12.5 distal forelimb nuclei stained with DAPI (blue) and the centromeric (red) and telomeric (green) TADs. (Scale bar, 1 μ m.) (C) Schematic (Left) and distributions (Right) of the various configurations observed by FISH in B. Prox and Dist, proximal and distal limb cells, respectively. (D) An example of structured illumination microscopy showing the absence of overlap between the two TADs. (Scale bar, 500 nm.) (E and F) Quantifications of the parameters observed under B. (E) Distances between the centers of both TADs. n.s., nonsignificant, using a Kruskall-Wallis test followed by Dunn's multiple comparison posttest. (F) Ellipticity measured for both the telomeric (left) and centromeric (right). * $P < 0.0001$, using unpaired t tests. (G) Position of the *HoxD* cluster for two alleles of a representative distal forelimb cell, using a fosmid probe specific for the genes *Hoxd8* to *Hoxd12* (green). The signal is scored between the centromeric (red) and telomeric (magenta) TADs. (Scale bar, 500 nm.) (Right) Close-ups of both alleles with white arrowheads showing an elongated *HoxD* cluster. (Scale bar, 200 nm.) (H-K) Distances between various probes localized within the *HoxD* cluster (H). (I) Forelimb cells nuclei stained with DAPI (blue) and DNA FISH (red and green) for different combinations of *Hoxd* fosmids (Top). (Scale bar, 500 nm.) (J) Quantification of the distribution of interprobe distances between selected pairs of probes. The statistical significance between datasets was tested using Kruskall-Wallis test followed by Dunn's multiple comparison posttest. All were significantly different ($P < 0.05$) except the ones indicated with n.s. See SI Appendix, Table S2 for details. (K) Frequency distribution of the measurements shown in J.

of the cluster and either its transcriptional activity or the presence of polycomb-associated proteins. For instance, the probe containing *Hoxd1* is covered by H3K27me3 marks in distal cells, whereas the *Hoxd8* to *Hoxd12* fragment shows a moderate coverage. In contrast, the probes encompassing either the *Hoxd11* to *Hoxd13* or the *Hoxd13* to *Evx2* DNA intervals are free of H3K27me3 in embryonic day (E) 12.5 distal and active cells, likely as a consequence of high transcriptional activity (Fig. 3A).

Each fosmid clone was labeled with the same Alexa 647 fluorophore and its signal analyzed by STORM microscopy. By comparing the signal morphologies (Fig. 3B), we noticed that the *Hoxd1* signals did not appear significantly more compact than the others (Fig. 3B; representative examples). If anything, this area of the *HoxD* cluster, which is densely covered by H3K27me3 marks, was slightly less circular than images obtained from the fosmids covering regions with lower amounts of H3K27me3 and highly expressed genes (Fig. 3C). To complement this observation, we labeled the two fosmid clones containing either the *Hoxd1* or the *Hoxd8* to *Hoxd12* regions, using Alexa 647 and Alexa 555, respectively, to directly assess their relative morphologies within the same cells. These experiments confirmed that these two DNA regions were decompact to similar extents in the same cells (SI Appendix, Fig. S2B). The most extensive elongation observed (*Hoxd8-d12*, Fig. 3B and C) matches the set of genes that was shown to have cell-specific long-range DNA contacts in the developing forelimb (16). To test whether decompaction could change with a modification of long-range contacts, we compared the two tissues in which the pattern of long-range interactions differs drastically: the proximal and distal forelimbs (Fig. 3D). Here we observed similar structures, both of them significantly more dispersed than that which was observed in the forebrain, used as a negative control (Fig. 3D).

We next investigated whether such a decompaction would also be observed in another tissue in which the *HoxD* cluster is strongly activated, and thus imaged the *Hoxd8-d12* region in the developing trunk. We compared forebrain cells in which the cluster is completely inactive, anterior trunk cells in which transcription occurs from *Hoxd1* to *Hoxd8* only, and posterior trunk cells in which *Hoxd1* to *Hoxd12* are activated. We observed the strongest decompaction in those tissue with the highest level of transcription (Fig. 3E), suggesting the existence of a link between transcription and the unfolded structure of *Hox* genes.

Effect of the Gene Deserts on Compaction. 4C studies using microdissected limb samples have indicated that parts of the *HoxD* cluster are strongly contacted by enhancer sequences located in both the centromeric and telomeric TADs (8, 16). Such strong enhancer contacts may exert forces upon the *HoxD* cluster, leading to variations in its global chromatin architecture. We assessed this possibility by analyzing three genetic perturbations in which *Hoxd* genes were separated from their respective enhancers by large targeted inversions (31, 32). The first allele was an inversion separating *HoxD* from its telomeric TAD by displacing the latter by 28 Mb (*Inv(AttP-*cd44**; Fig. 3F), which switched off *Hoxd9-11* in proximal limb cells and decreased their transcription in distal limb cells. The morphologies of signals detected when using this large inversion were as elongated as in noninverted cells, showing that the immediate regulatory neighborhood, even though it contains sequences interacting with the probe, was not critical in the shaping of the cluster, at least in these particular conditions. In both the inverted and wild-type loci, a low circularity index was determined for the *Hoxd8* to *Hoxd12* DNA region (Fig. 3G and H), suggesting that the presence of genuine enhancer sequences and constitutive interactions (16) is not necessary for the decompaction of the *HoxD* cluster.

We also assessed the *Inv(Nsi-Itga6)* centromeric inversion (SI Appendix, Fig. S3 A and B), which repositions the centromeric regulatory sequences several Mb away from the cluster, thus abrogating all specific enhancer–promoter interactions occurring during digit development and, consequently, turning off *Hoxd*

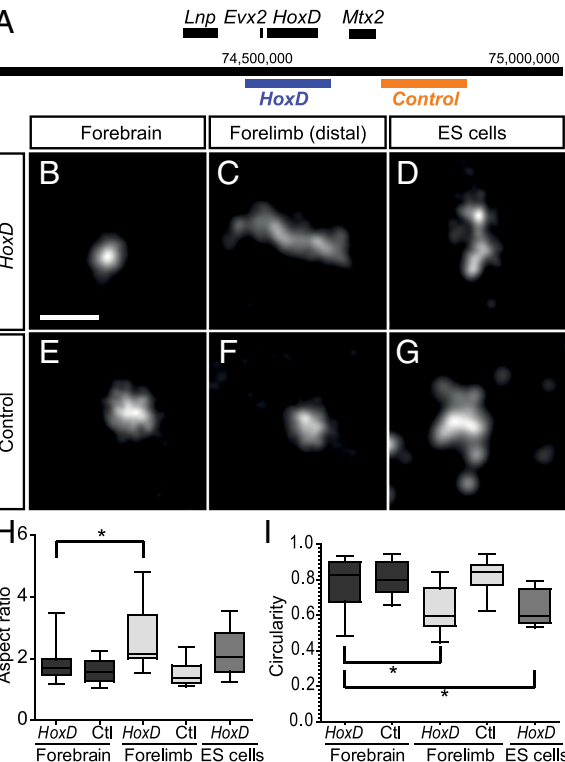


Fig. 2. Distinct conformations of the *HoxD* cluster visible by STORM microscopy. (A) Schematic view of the two BAC clones, 160 and 175 kb large, respectively, used to visualize the *HoxD* cluster and part of the telomeric gene desert, using STORM imaging. (B–G) DNA FISH using Alexa 647 and resolved through STORM, using either “inactive” forebrain (B and E), “active” distal forelimb (C and F), or synchronized ES (D and G) cells. (Scale bar, 200 nm.) (H and I) For the same cells, quantifications of aspect ratio (H) and circularity (I) are shown, where the asterisk indicates $P < 0.01$, using a Kruskall-Wallis test followed by Dunn’s multiple comparison posttest (see SI Appendix, Materials and Methods).

genes transcription (33). Again, the decompacted aspect of the *HoxD* cluster was not dramatically modified after STORM imaging (SI Appendix, Fig. S3B). Finally, we used a large inversion, with a breakpoint located between *Hoxd10* and *Hoxd11*, thus splitting the *HoxD* cluster into two parts, leaving in place only from *Hoxd11* to *Hoxd13* and their centromeric gene desert (ref. 31; scheme in SI Appendix, Fig. S3). We monitored the aspect ratio of the short remaining cluster, using the fosmid probe covering from *Hoxd11* to *Hoxd13*, and found no difference in elongation (SI Appendix, Fig. S3C), suggesting a full *HoxD* cluster is not critical to spatially organizing chromatin in its various parts.

Discussion

The organization of chromatin in the nuclear space is a critical parameter for the proper control of transcription, and the extent of chromatin elongation at a given genetic locus may reflect its capacity to be efficiently transcribed (34). We previously determined that the *HoxD* gene cluster was the target of a bimodal type of global regulation, exerted from either the telomeric or centromeric gene deserts, two regulatory landscapes matching TADs, and separated by the *HoxD* cluster itself (9, 16). However, chromosome conformation capture-based experiments average the treatment of several million independent cells, and the presence of dense and compact chromatin architectures flanking the *HoxD* cluster remained to be shown at the cellular level. Here, by concomitantly labeling series of BACs spanning specifically the two TADs, we demonstrate that such configurations indeed exist as dense and separate objects in individual cells, as

previously seen on a specific locus at the X-chromosome (10), with a low level of partial overlap consistent with the reduced number of interactions observed in 4C between the two TADs (16, 17). This observation was confirmed by structured illumination microscopy. The distances between TADs were comparable between cells, whether or not they expressed *HoxD* genes, supporting the existence of a poised regulatory structure already present in the absence of transcription (8). However, the direct visualization of TADs at this locus is not informative regarding potential fluctuations in contacts within each TAD, from one cell to another (20). It nevertheless demonstrates that such dense structures exist in all cells and on both alleles.

By using super-resolution microscopy (STORM), we scored the most extensively elongated forms in cells from either the developing distal forelimb or the posterior trunk, two tissues in which several *Hoxd* genes are strongly active. In contrast, dense and compact structures were scored either in brain cells, negative for all *Hox* gene transcription at this stage, or when using a control probe located outside the gene cluster. These elongated morphologies generally occurred along a major axis and appeared continuous, either when using large probes covering the whole cluster or with smaller probes detecting only one or a few genes. In distal forelimb cells, however, where the *Hoxd1* to *Hoxd4* region is covered by H3K27me3 chromatin marks (16), we did not observe any significant asymmetric compaction. In contrast, the inactive part of the *HoxD* cluster was at least as elongated as the transcriptionally active region. One explanation for this unexpected observation may be the robust and nonproductive contacts established by *Hoxd1* with the telomeric TAD (16), which may lead to tensions elongating the gene cluster (see following).

A significant elongation of the gene cluster was also scored in ES cells, even though the entire *HoxD* cluster is labeled with both H3K4me3 and H3K27me3 chromatin marks (22, 28, 30) associated with the formation of local chromatin domains (23, 35), in contrast with the idea that *Hox* clusters adopt a “closed” conformation whenever genes are silent (23). In ES cells, however, the 4C interaction patterns are much weaker than in brain cells (35), probably because of the presence of bivalent chromatin marks and the concomitant reduced amount of H3K27me3 modifications [Fig. 1 and figure S1 in ref. 35, the latter being even weaker when ES cells were cultured in 2i medium (36)]. It was also noticed that *Hoxd* genes established many more interactions with the neighboring gene deserts in ES cells than in brain cells (35), where most interactions involved the gene cluster itself, further suggesting a more decompact configuration of the locus in ES cells. Therefore, the vast majority of ES cells may display decompact chromatin at their *Hox* loci. The presence of some H3K27me3-labeled nucleosomes may induce enough transitory interactions to be translated into read counts after deep sequencing of 4C products.

Altogether, these data suggest that in the developing limbs, the *HoxD* cluster is decompact, with an elongated shape including both active and inactive genes. Therefore, the coverage of specific parts of the cluster by polycomb complexes, depending on the proximal versus distal position of the cells (8, 16) and observed in other functional contexts (30, 37, 38), does not seem to significantly influence its level of compaction. The distances apparently associated with these elongated forms correspond to previous distance predictions established by mathematical modeling (29). Stretching events associated with transcription were also reported, which seem to occur within this range of elongation lengths (5), and several recent studies either describe or predict distances ranging from 300 to more than 1,000 nm (39, 40). The elongation of the *HoxD* cluster in limb cells despite its partial labeling by H3K27me3 may reflect an influence from the flanking TADs in extending the structure in both directions, following either productive or constitutive interactions. We evaluated this possibility by using three large inversions modifying the global relationships between the gene cluster and its two regulatory landscapes. However, none of these rearrangements did affect the capacity of the cluster to elongate. If anything, elongation

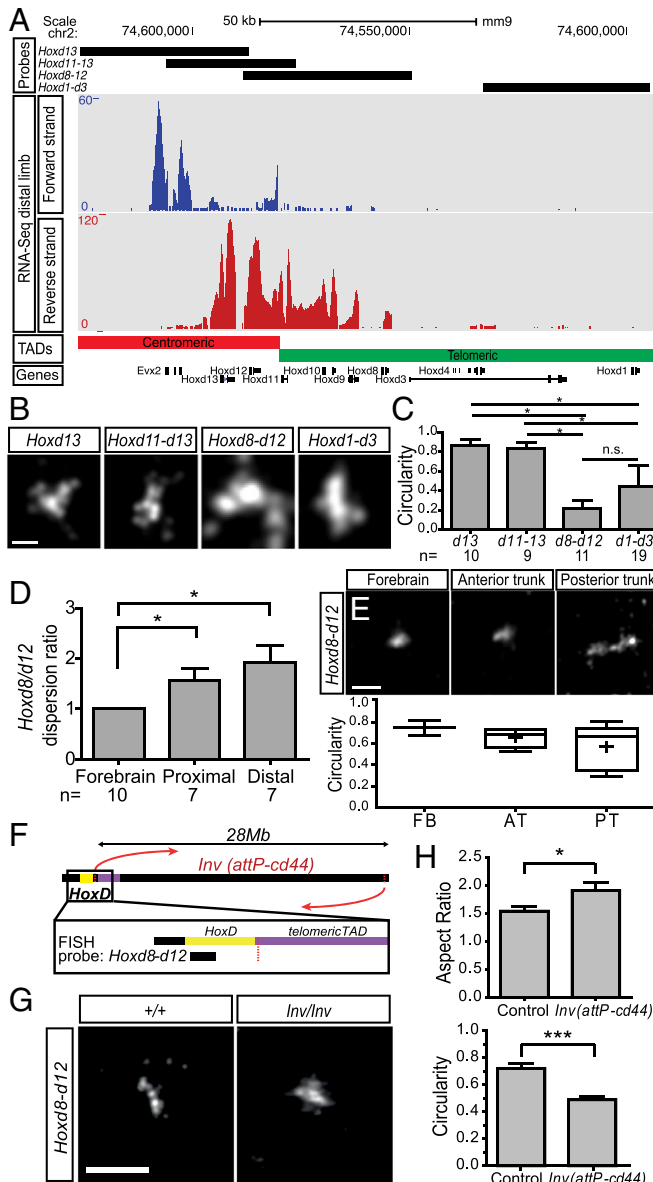


Fig. 3. STORM analysis using smaller probes in different control and mutant tissues. (A) RNA profile of distal forelimb cells showing the expression of *Hoxd8* to *Hoxd13* (red) aligned with the positions of four fosmid probes (black, Top). The boundary between the centromeric (red) and telomeric (green) TADs is shown below, as well as the transcription of *Evx2* from the other DNA strand (blue). (B) STORM imaging using the four probes under A and their relative circularity index (C). (Scale bar, B, 100 nm.) (D) Refined analysis of the *Hoxd8* to *Hoxd12* probe in forebrain, proximal limb, and distal limb cells, quantifying the level of dispersion as depicted in C and *SI Appendix*, Fig. S2B. (Scale bar, 200 nm.) (E) STORM imaging of the *Hoxd8* to *Hoxd12* probe in E10.5 embryos in cells positioned along the anterior to posterior axis. AT, anterior trunk; FB, forebrain; PT, posterior trunk. (Scale bar, 200 nm.) (F) Scheme of the 28-Mb large *Inv(attP-cd44)* inversion (red arrows) removing the telomeric TAD (purple), and location of the *Hoxd8* to *Hoxd12* probe (black). (G) STORM imaging of the *Hoxd8* to *Hoxd12* region in E12.5 distal forelimb cells from either a homozygous *Inv*(*attP-cd44*) embryo (Right) or control littermate (Left). (Scale bar, 200 nm.) (H) Quantification of the aspect ratio and circularity in both configurations shown under G. * $P < 0.05$ and *** $P < 0.001$, using Mann-Whitney *U* test. In C and D, ** $P < 0.01$, using a Kruskall-Wallis test followed by Dunn's multiple comparison posttest. n.s., not significant.

was more pronounced and the circularity index lower, suggesting the telomeric gene desert may participate in the compaction of the system, rather than its elongation.

In this context, it is noteworthy that the part of the cluster displaying the highest level of decompaction was the *Hoxd8* to *Hoxd12* region, which precisely matches with the inter-TADs boundary (9, 16). This particular region of *HoxD*, located between genes strongly and constitutively interacting with either the centromeric (*Hoxd13*) or the telomeric (*Hoxd1*, *Hoxd4*) TADs, may thus display more flexibility, perhaps reflected by the capacity of *Hoxd8* or *Hoxd12* to switch their contacts from one TAD to the other in various limb cell-types (16). Interestingly, this region is strongly enriched in binding sites for architectural proteins such as CCCTC-binding factor (CTCF) and cohesin (41, 42), which are known for their capacity to organize genomic boundaries and domains, in particular at TAD boundaries (43). Whether the presence of several sites bound by CTCF in the sequence targeted by the *Hoxd8* to *Hoxd12* fosmid play a role in the elongation observed by STORM remains to be tested, however, as CTCF-driven interactions would be expected to increase compaction, rather than the opposite. An alternative explanation is that the resolution of our STORM approach, although allowing a clear distinction between fully compacted and decompactated *Hox* clusters, may not easily detect mixed configurations, in particular when only a small part of the cluster differs in shape from the rest.

In conclusion, these data suggest the structural organization of the *HoxD* gene cluster may predate transcriptional activation and may subsequently be rather independent from its transcriptional status. Perhaps such an elongated structure is maintained in cells expressing subsets of *HoxD* genes, whereas compaction occurs in those cells where genes are silent, such as the fetal brain. In this latter tissue indeed, an elongated structure was never observed. By using 2D and 3D FISH, it was previously reported that a decompaction of the *HoxD* cluster occurs in ES cells that are differentiating in vitro, and that this process is linked to the progressive reduction in levels of PRC1 components (22). With the resolution of our STORM approach, the *HoxD* cluster did not appear to adopt a compact structure, which would be released on differentiation. It is possible that the spatial architecture of a decondensed cluster differs only slightly between the active and inactive states, leading to the observation of a range of distances between localized probes used for FISH. The presence of polycomb complexes may, for instance, impose such distinct organizations of the *HoxD* cluster in space, while having little influence on its general level of compaction. In this context, a detailed analysis of these structures by super-resolution microscopy in ES cells mutant for components of either the PRC1 or PRC2 complexes may be informative.

Materials and Methods

All experiments involving animals were performed in agreement with the Swiss law on animal protection, with the appropriate legal authorizations to D.D. Tissues were isolated from E10.5 or E12.5 embryos, either wild-type or mutant for the *Inv(Nsi-Itga6)*, *Inv(attP-cd44)*, and *Inv(HoxD^{RVIII}-Cd44)* inversions (31). Mouse ES cells were grown in serum with 1,000 U/mL leukemia inhibitory factor under feeder-free conditions and G1-synchronized through mitotic shake off. 3D DNA FISH was as in ref. 5. Structured illumination images were acquired using a Nikon structured illumination microscopy setup (Eclipse T1 microscope fitted with a super-resolution Apochromat total internal reflection fluorescence 100 \times /1.49 NA objective IXON3 camera; Andor Technology). For STORM imaging, DNA FISH samples were imaged using a UPlanSApo 100 \times /1.40 oil objective (Olympus), and typically 10,000–15,000 snapshot images with a pixel size of 100 nm and an exposure time of 0.03 s were acquired to create one super-resolution (SR) image. SR images were reconstructed with the Octane software (44), and statistical differences between samples were evaluated with the Kruskall-Wallis test, followed by Dunn's multiple comparison posttest, with the exception of Fig. 3H (Mann-Whitney *U* test). RNA-Seq was performed according to the Truseq Stranded Illumina protocol, with polyA selection. The reads were mapped to Ensembl Mouse assembly National Center for Biotechnology Information Mouse Assembly 37 (mm9) and translated into reads per gene (RPKM) using the Bioinformatics and Biostatistics Core Facility (BBCF), High-Throughput Sequencing station (available at htsstation.epfl.ch). An extended description of the materials, methods, and data analysis is provided in the *SI Appendix*.

ACKNOWLEDGMENTS. We thank the members of the D.D. laboratories for discussions and S. Boyle and W. Bickmore (Medical Research Council Edinburgh) for their help with setting up the FISH procedures. We also thank O. Burri and R. Guiet [Ecole Polytechnique Fédérale de Lausanne (EPFL)] for assistance with image analysis and T. Laroche for help with structured illumination microscopy, as well as B. Mascrez and S. Gitto for help with mutant stocks. We thank the

Geneva Genomics Platform (University of Geneva) and the Bioinformatics and Biostatistics Core Facility (EPFL) in Lausanne for their assistance with RNA-Seq. This work was supported by funds from the EPFL, the University of Geneva, the Swiss National Research Fund, the European Research Council (ERC) Grant SystemsHox.ch, and the Claraz Foundation (to D.D.), as well as Swiss National Research Fund Grant CR33I2_149850 and ERC Grant PALMassembly (to S.M.).

1. Bickmore WA, van Steensel B (2013) Genome architecture: Domain organization of interphase chromosomes. *Cell* 152(6):1270–1284.
2. de Laat W, Duboule D (2013) Topology of mammalian developmental enhancers and their regulatory landscapes. *Nature* 502(7472):499–506.
3. Gorkin DU, Leung D, Ren B (2014) The 3D genome in transcriptional regulation and pluripotency. *Cell Stem Cell* 14(6):762–775.
4. Chambeillon S, Bickmore WA (2004) Does looping and clustering in the nucleus regulate gene expression? *Curr Opin Cell Biol* 16(3):256–262.
5. Morey C, Da Silva NR, Perry P, Bickmore WA (2007) Nuclear reorganisation and chromatin decondensation are conserved, but distinct, mechanisms linked to Hox gene activation. *Development* 134(5):909–919.
6. van de Corput MP, et al. (2012) Super-resolution imaging reveals three-dimensional folding dynamics of the β -globin locus upon gene activation. *J Cell Sci* 125(Pt 19): 4630–4639.
7. de Laat W, Dekker J (2012) 3C-based technologies to study the shape of the genome. *Methods* 58(3):189–191.
8. Montavon T, et al. (2011) A regulatory archipelago controls Hox genes transcription in digits. *Cell* 147(5):1132–1145.
9. Dixon JR, et al. (2012) Topological domains in mammalian genomes identified by analysis of chromatin interactions. *Nature* 485(7398):376–380.
10. Nora EP, et al. (2012) Spatial partitioning of the regulatory landscape of the X-inactivation centre. *Nature* 485(7398):381–385.
11. Nora EP, Dekker J, Heard E (2013) Segmental folding of chromosomes: A basis for structural and regulatory chromosomal neighborhoods? *BioEssays* 35(9):818–828.
12. Schwarzer WV, Spitz F (2014) The architecture of gene expression: Integrating dispersed cis-regulatory modules into coherent regulatory domains. *Curr Opin Genet Dev* 27:74–82.
13. Lonfat N, Duboule D (April 23, 2015) Structure, function and evolution of topologically associating domains (TADs) at HOX loci. *FEBS Lett*, 10.1016/j.febslet.2015.04.024.
14. Woltering JM, Noordermeer D, Leleu M, Duboule D (2014) Conservation and divergence of regulatory strategies at Hox Loci and the origin of tetrapod digits. *PLoS Biol* 12(1):e1001773.
15. Berlivet S, et al. (2013) Clustering of tissue-specific sub-TADs accompanies the regulation of HoxA genes in developing limbs. *PLoS Genet* 9(12):e1004018.
16. Andrey G, et al. (2013) A switch between topological domains underlies HoxD genes collinearity in mouse limbs. *Science* 340(6137):1234167.
17. Lonfat N, Montavon T, Darbellay F, Gitto S, Duboule D (2014) Convergent evolution of complex regulatory landscapes and pleiotropy at Hox loci. *Science* 346(6212):1004–1006.
18. Montavon T, Duboule D (2013) Chromatin organization and global regulation of Hox gene clusters. *Philos Trans R Soc Lond B Biol Sci* 368(1620):20120367.
19. Delpretti S, et al. (2013) Multiple enhancers regulate Hoxd genes and the Hotdog lncRNA during cecum budding. *Cell Reports* 5(1):137–150.
20. Giorgetti L, et al. (2014) Predictive polymer modeling reveals coupled fluctuations in chromosome conformation and transcription. *Cell* 157(4):950–963.
21. Williamson I, et al. (2014) Spatial genome organization: Contrasting views from chromosome conformation capture and fluorescence in situ hybridization. *Genes Dev* 28(24):2778–2791.
22. Eskeland R, et al. (2010) Ring1B compacts chromatin structure and represses gene expression independent of histone ubiquitination. *Mol Cell* 38(3):452–464.
23. Noordermeer D, et al. (2011) The dynamic architecture of Hox gene clusters. *Science* 334(6053):222–225.
24. Manley S, Gunzenhäuser J, Olivier N (2011) A starter kit for point-localization super-resolution imaging. *Curr Opin Chem Biol* 15(6):813–821.
25. Huang B, Wang W, Bates M, Zhuang X (2008) Three-dimensional super-resolution imaging by stochastic optical reconstruction microscopy. *Science* 319(5864):810–813.
26. Benke A, Manley S (2012) Live-cell dSTORM of cellular DNA based on direct DNA labeling. *ChemBioChem* 13(2):298–301.
27. Montavon T, Le Garrec J-F, Kerszberg M, Duboule D (2008) Modeling Hox gene regulation in digits: Reverse collinearity and the molecular origin of thumbness. *Genes Dev* 22(3):346–359.
28. Bernstein BE, et al. (2006) A bivalent chromatin structure marks key developmental genes in embryonic stem cells. *Cell* 125(2):315–326.
29. Papageorgiou S (2006) Pulling forces acting on Hox gene clusters cause expression collinearity. *Int J Dev Biol* 50(2-3):301–308.
30. Soshnikova N, Duboule D (2009) Epigenetic temporal control of mouse Hox genes in vivo. *Science* 324(5932):1320–1323.
31. Spitz F, Herkenne C, Morris MA, Duboule D (2005) Inversion-induced disruption of the HoxD cluster leads to the partition of regulatory landscapes. *Nat Genet* 37(8):889–893.
32. Tschopp P, Duboule D (2014) The genetics of murine Hox loci: TAMERE, STRING, and PANTHERE to engineer chromosome variants. *Methods Mol Biol* 1196:89–102.
33. Tschopp P, Duboule D (2011) A regulatory ‘landscape effect’ over the HoxD cluster. *Dev Biol* 351(2):288–296.
34. Bickmore WA (2013) The spatial organization of the human genome. *Annu Rev Genomics Hum Genet* 14:67–84.
35. Noordermeer D, et al. (2014) Temporal dynamics and developmental memory of 3D chromatin architecture at Hox gene loci. *eLife* 3:e02557.
36. Marks H, et al. (2012) The transcriptional and epigenomic foundations of ground state pluripotency. *Cell* 149(3):590–604.
37. Phillips-Cremins JE, et al. (2013) Architectural protein subclasses shape 3D organization of genomes during lineage commitment. *Cell* 153(6):1281–1295.
38. Ferraiuolo MA, et al. (2010) The three-dimensional architecture of Hox cluster silencing. *Nucleic Acids Res* 38(21):7472–7484.
39. Song F, et al. (2014) Cryo-EM study of the chromatin fiber reveals a double helix twisted by tetranucleosomal units. *Science* 344(6182):376–380.
40. Zhang B, Wolynes PG (2015) Topology, structures, and energy landscapes of human chromosomes. *Proc Natl Acad Sci USA* 112(19):6062–6067.
41. Soshnikova N, Montavon T, Leleu M, Galjart N, Duboule D (2010) Functional analysis of CTCF during mammalian limb development. *Dev Cell* 19(6):819–830.
42. Gómez-Díaz E, Corces VG (2014) Architectural proteins: Regulators of 3D genome organization in cell fate. *Trends Cell Biol* 24(11):703–711.
43. Van Bortle K, et al. (2014) Insulator function and topological domain border strength scale with architectural protein occupancy. *Genome Biol* 15(6):R82.
44. Niu L, Yu J (2008) Investigating intracellular dynamics of FtsZ cytoskeleton with photoactivation single-molecule tracking. *Biophys J* 95(4):2009–2016.

Title: Nanoscale spatial organization of the *HoxD* gene cluster in distinct transcriptional states

Authors: Pierre J. Fabre¹, Alexander Benke², Elisabeth Joye¹, Thi Hanh Nguyen Huynh³, Suliana Manley^{2,*} and Denis Duboule^{1,3,*}

¹School of Life Sciences, Ecole Polytechnique Fédérale, Lausanne, 1015 Lausanne, Switzerland, ²Laboratory of Experimental Biophysics, Ecole Polytechnique Fédérale de Lausanne 1015 Lausanne, Switzerland, ³Department of Genetics and Evolution, University of Geneva, 1211 Geneva 4, Switzerland.

Supplemental material

Content

Full methods

Supplemental figures S1 to S8 with legends

Supplemental table S1 to S3

Full Methods

Animal care, tissue sampling

All experiments involving animals were performed in agreement with the Swiss law on animal protection (LPA) with the appropriate legal authorizations to D.D. Tissue samples were isolated at embryonic day 10.5 (E10.5), with day E0.5 being noon on the day of the vaginal plug. E12.5 specimen homozygous for either the Inv(*Nsi-Itga6*) and Inv(*attP-cd44*) or E10.5 specimen homozygous for the Inv(*HoxD^{RVIII}-Cd44*) alleles (Spitz et al., 2005) were obtained by crossing mice trans-heterozygous for each allele. Control E12.5 or E10.5 forebrains were obtained from wild type littermates.

ES cell culture and synchronization

Mouse H1 ES cells (Dierich and Dolle, 1997) were grown on gelatinized plates under feeder-free conditions in Dulbecco's modified Eagle's medium (DMEM, Life Technologies) supplemented with 10% fetal calf serum, non-essential amino acids (Life Technologies), Pen–Strep (Life Technologies), Sodium Pyruvate (Life Technologies), 0.1 mM β-mercaptoethanol and 1000 U/ml Leukemia inhibitory factor (LIF). In order to rule out the possibility that the detection of stretched conformations of the *HoxD* cluster were associated with DNA replication events, we synchronized the ES cells through a mitotic shake off. ES cells were subsequently plated on 18-mm size 1.5 precision coverslips (Carl Roth GmbH), coated with poly-L-lysine.

DNA-FISH

DNA fluorescent *in situ* hybridization was conducted as previously described (Vieux-Rochas et al., 2015). E10.5 or E12.5 mouse embryos were fixed in 4% paraformaldehyde, embedded in paraffin blocks and cut at 6 µm. Sections were oriented such that cells belonging either to the distal or proximal parts of the growing limb bud could be unambiguously discriminated. ES cells were fixed with 4% paraformaldehyde for 10 minutes. Probes were prepared by nick-translation with either biotin- or digoxigenin-UTP using fosmid and BAC clones obtained from the BACPAC Resources Center (<https://bacpac.chori.org/>). 100 ng (fosmid) or 200 ng

(BAC) of DNA were used with 7 µg of Cot1-DNA and 10 µg of sonicated salmon sperm DNA.

For the labeling of entire TADs, several consecutive BACs covering most of the TAD sequences were used concomitantly. They were labeled using either digoxigenin- or biotin-dUTP by nick translation with fluorescent revelations as described previously (Morey et al., 2007). TAD-FISH presented in Fig. 1B-G were labeled using either Alexa 647 or Alexa 568 with dye swap to ensure that the changes in ellipticity presented in Fig. 1F was not due to a specific dye. DNA-FISH shown in Fig. 1I-K were labeled using Alexa 647 and Alexa 568 following the conditions presented in Table S3. STORM signals were detected after labelling using either Alexa 647 or Alexa 555 as fluorophores, due to their higher efficiency to detect single molecules blinking signals required for STORM imaging. Slides were stained with DAPI and mounted in ProLong Gold (Life Technologies).

3D Multi-color DNA-FISH imaging

Images shown in Fig. 1B, 1G and 1I were acquired using a 60X Plan-Apo objective (numerical aperture of 1.42) and a B/W CCD ORCA ER B7W Hamamatsu camera associated with an inverted Olympus IX81 microscope. The image stacks with a 200 nm step were saved as TIFF stacks. Image reconstruction and deconvolution were performed using FIJI (NIH, ImageJ v1.47q; <http://fiji.sc/Fiji>) and Huygens Remote Manager (Scientific Volume Imaging, version 3.0.3).

Distance measurements between probe signals and their ellipticities were determined using an automated spot/surface detection algorithm followed by visual verification and manual correction using IMARIS version 6.5, Bitplane AG and Matlab 7.5, MathWorks SA. For these measurements in standard widefield microscopy, chromatic shift between the two fluorophores were assessed using tetraspeck beads and shown to be lower than a pixel. Statistical significance analyses of distances were performed using an unpaired two-sample t-test and using the Kruskal-Wallis test followed by Dunn's post test.

Analysis of conformations and morphological parameters

The analysis of TAD-FISH in Fig. 1C shows the distribution of the different conformations observed (spaced, contact or partial overlap), was conducted by three

different observers, under blind conditions. The analysis shown in figure S1E was also blinded, with only two conformations scored: either segregated or mixed.

The analyses of shapes were defined using three main parameters: aspect ratio, circularity and ellipticity. They were assessed after the replacement of their area selection with the best fit ellipse. Aspect ratio and circularity were quantified using Fiji (NIH, ImageJ v1.47q). Circularity is defined as

$$4\pi \times \frac{[\text{Area}]}{[\text{Perimeter}]^2}$$

with the maximal value (1) indicating a perfect circle. As the value approaches 0.0, it indicates an increasingly elongated shape. The aspect ratio was calculated as a ratio between major and minor axes of ellipse fitted to the shape of the cluster. It was defined as

$$\frac{[\text{Major axis}]}{[\text{Minor axis}]}$$

The ellipticity was defined as

$$\frac{[\text{Major axis- minor axis}]}{[\text{Major axis}]}$$

with the maximal value, 1.0, indicating a perfect ellipse. It was scored using the IMARIS (v6.5, Bitplane AG) software and quantified automatically. The dispersion ratio shown in figure 3D is the measure of the number of objects observed for each cluster with the lowest value 1.0, indicates a single object.

SIM Imaging

Structured illumination images were acquired using a Nikon SIM setup (Eclipse T1 microscope fitted with a super-resolution Apochromat total internal reflection fluorescence 100 \times / 1.49 NA objective and an electron-multiplying charge-coupled device camera (IXON3; Andor Technology).

Imaging was performed in 3D SIM acquisition mode with 3 dyes (DAPI, Alexa 568 and Alexa 647), which were excited with fixed wavelength using coherent Cube at 100mW (for 402nm and 561 excitations) and a coherent Jive at 158mW (for 641nm excitation). Image reconstruction was performed using the NIS-Elements software (Nikon; based on Gustafsson et al., 2008) and reconstruction parameters were as follows: Contrast: 0.70, apodization: 1.00 and Widh3DFilter: 0.20.

STORM imaging

STORM imaging was performed on a modified Olympus IX-71 inverted microscope equipped with an oil objective (Olympus, UPlanSApo 100x, 1.40 NA) and a piezo objective scanner (Physik Instrumente, P-725, PIFOC). Fluorescence was excited by a 641nm laser (Coherent, Cube 640nm-100C) with an irradiance of 10-20 kW cm⁻². For photoreactivation we also used 405 nm (Coherent, Cube 405nm-100C) laser with an irradiance < 0.05 kW cm⁻². Emitted light was directed through a dichroic mirror (89100BS, Chroma) and emission filter (ET700/75m, Chroma) and imaged by an EMCCD camera (Andor Technology, iXon+).

To induce photoswitching, samples were imaged in GLOX buffer (0.5 mg.ml⁻¹ glucose oxidase (Sigma-Aldrich G0543-10KU)), 40 mg ml⁻¹ catalase (Sigma-Aldrich C3515) and 10% glucose (Sigma-Aldrich G8270). For each imaging session, GLOX buffer was freshly prepared, then after 30 min of equilibration, β-mercaptoethanol (Sigma-Aldrich M6250) was added for a final concentration of 143 μM. The pH of the solution was adjusted to 8-8.5 using HEPES (Sigma-Aldrich H3662). Stacks of 10000-15000 images with a pixel size of 100 nm with exposure time 0.03 s were acquired to create each STORM image.

STORM Data analysis

Initially, *HoxD* clusters were identified using standard deviation (STD) images from the raw image stacks. Each pixel value in the STD image was determined by calculating the standard deviation of intensity values across the image stack. Spots with a signal approximately 10x higher than other objects within the nucleus in STD images were considered as labeled clusters; this first segmentation step enabled us to avoid analyzing non-specific staining (Fig. S3A). After this step, we always obtained less than or equal to 4 bright spots per cell, consistent with the maximum expected number of clusters per cell. In addition, we performed several multicolor standard microscopy experiments with probes used for SR imaging. These experiments confirmed the specificity of staining. Probes that were close to each other on genome were also close to each other in physical space in cells (Fig. S3).

Octane software was used to analyze raw image stacks and reconstruct STORM images, which were later used for morphological analysis. During image reconstruction, the single molecule peak detection threshold was set individually for

each sample set, due to variation in image background intensity. The threshold was chosen using the following qualitative criteria. We required that the majority of bright fluorescent spots corresponding to single molecules that we manually detected based of their shape and size in the cluster region, were also detected by the software. This procedure is illustrated in Fig. S3.

To account for molecules that are fluorescent for several frames, we performed grouping. Localizations were grouped as belonging to the same molecule if the distance between them in space was less than 100 nm (grouping radius) and in time less than two frames (grouping gap). These parameters allowed accounting for most of the molecules that are on for several frames. Octane software allows visual inspection of grouped localizations so we checked that grouping was done properly by manually inspecting grouped localizations on test samples for each dataset. The choice of grouping parameters is further discussed (Fig. S4).

Typical precision in position determination of the molecule (localization precision) that we obtained in our experiments was around 40 nm (as measured with Peakselector software). Based on this we set a pixel size of 10 nm in reconstructed STORM images to slightly oversample the data. STORM images were rendered in the following way: each localized molecule was represented as a spot whose width reflected the mean localization precision for the dataset, usually 40 nm. We found that moderately changing these two rendering parameters (pixel size and spot size) didn't change the visual appearance or measured geometric parameters of cluster (Fig. S5).

The shape of identified clusters was determined using thresholding of rendered STORM images. The thresholding was performed with Otsu's algorithm integrated into Fiji software (<http://fiji.sc/Fiji>). The algorithm sets a threshold by minimizing a weighted sum of variances of the background class and the image class pixels. The results of Otsu algorithm are demonstrated (Fig. S6). The resulting thresholded image then was used to determine the aspect ratio of clusters. The aspect ratio was calculated as a ratio between major and minor axes of ellipse fitted to the shape of the cluster. To evaluate statistical differences between samples, we used the two-sample t-test for means.

It should be noted that the ellipticities we measured are an underestimation of the true elongation of the *HoxD* clusters. This is because we performed 2D imaging to avoid distortion of clusters in the axial dimension, an effect that arises due to the poorer localization precision in z. Therefore, our images represent a projection of 3D

clusters, which can be oriented with different angles with respect to the 2D imaging plane (Fig. S8). If we assume that an elongated object is randomly oriented in space we can estimate in the simplest case that the average real 3D elongation is $(\pi/2) \sim 1.57$ larger than the average measured 2D elongation.

RNA-Sequencing

E12.5 distal forelimbs were dissected and isolated using Trizol LS reagent (Life Technologies) to generate total RNA tissue samples. RNA-Seq was performed according to the TruSeq Stranded Illumina protocol, with polyA selection. The strand-specific total RNA-seq libraries were constructed according to the manufacturers instructions (Illumina). Sequencing was done using 100 bp Single end reads on the Illumina HiSeq system according to the manufacturer's specifications. RNA-seq reads were mapped to ENSEMBL Mouse assembly NCBIM37 (mm9) and translated into reads per gene (RPKM) using the RNA-Seq pipeline of the Bioinformatics and Biostatistics Core Facility (BBCF) HTSstation (available at <http://htsstation.epfl.ch>). RNA-seq data is available from the Gene Expression Omnibus (GEO) repository under accession number GSE72285.

References

1. Spitz F, Herkenne C, Morris MA, & Duboule D (2005) Inversion-induced disruption of the Hoxd cluster leads to the partition of regulatory landscapes. *Nat Genet* 37(8):889-893.
2. Dierich A & Dolle P (1997) Gene targeting in embryonic stem cells. *Methods in Developmental Toxicology and Biology*:111-123.
3. Vieux-Rochas M, Fabre PJ, Leleu M, Duboule D, & Noordermeer D (2015) Clustering of mammalian Hox genes with other H3K27me3 targets within an active nuclear domain. *Proceedings of the National Academy of Sciences of the United States of America* 112(15):4672-4677.
4. Morey C, Da Silva NR, Perry P, & Bickmore WA (2007) Nuclear reorganisation and chromatin decondensation are conserved, but distinct, mechanisms linked to Hox gene activation. *Development* 134(5):909-919.
5. Gustafsson MG, et al. (2008) Three-dimensional resolution doubling in wide-field fluorescence microscopy by structured illumination. *Biophysical journal* 94(12):4957-4970.
6. Andrey G, et al. (2013) A switch between topological domains underlies HoxD genes collinearity in mouse limbs. *Science* 340(6137):1234167.
7. Dixon JR, et al. (2012) Topological domains in mammalian genomes identified by analysis of chromatin interactions. *Nature* 485(7398):376-380.

Supplemental figures and legends

Supplemental Figure S1

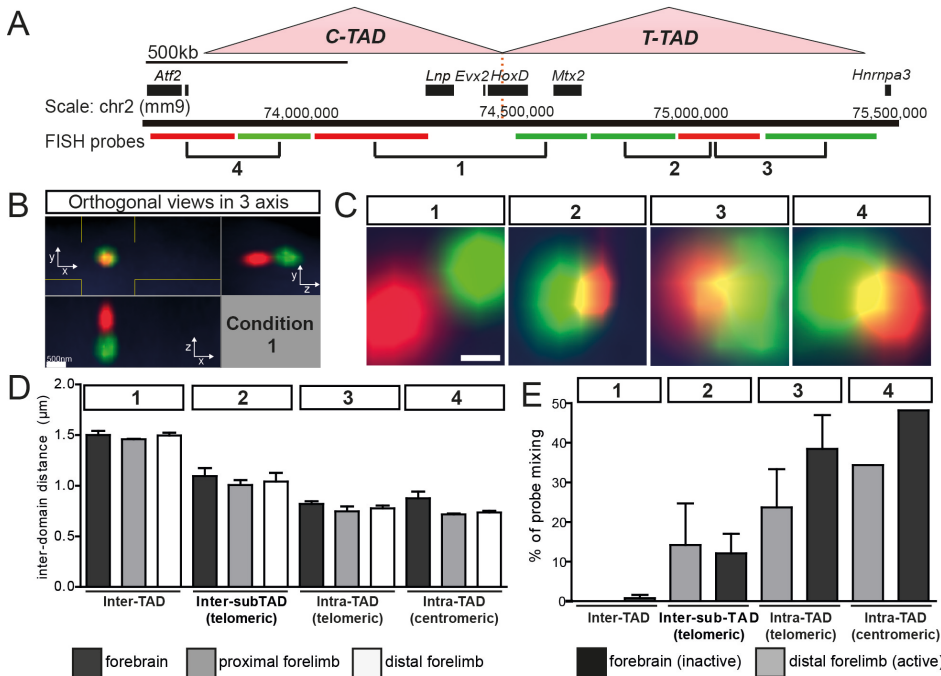


Figure S1: Overlapping capacity between probes in and out of the TAD units.

(A) Schematic of the probe positions as shown in Fig. 1 with the combinations (1 to 4) used for the 3D-DNA FISH. The dotted line represents the TAD boundary as defined in (9). (B) Overlaps were assessed using reconstructed 3D image using Imaris software. The picture is an orthogonal view of a slice showing a combination of BACs (condition 1) that appear overlapping in 2D but were scored segregated when visualized in three dimensions. Scale bar: 500nm (C) Each image shows the extent of overlap observed for each combination tested. Scale bar: 200nm. (D) Quantification of the distances between two probes for each of the combination tested. For each combination is shown the average distance in three different embryonic tissue: E12.5 forebrain (dark grey), proximal forelimb (light grey) and distal forelimb (white). N>100 for each pair including data from 2 different experiments (conditions 1 to 3) or one experiment (condition 4). Error bars denote SD. (E) Blinded and qualitative measurement to show the percentage of pairs (70 to 100 pairs) that overlap. As shown in (B) the pairs were not scored as mixed if they were segregated in 3D. The errors bars for conditions 1 to 3 denote SD (n=2 for each). The measurements for condition 4 came from the same animal (n=1).

Supplemental Figure S2

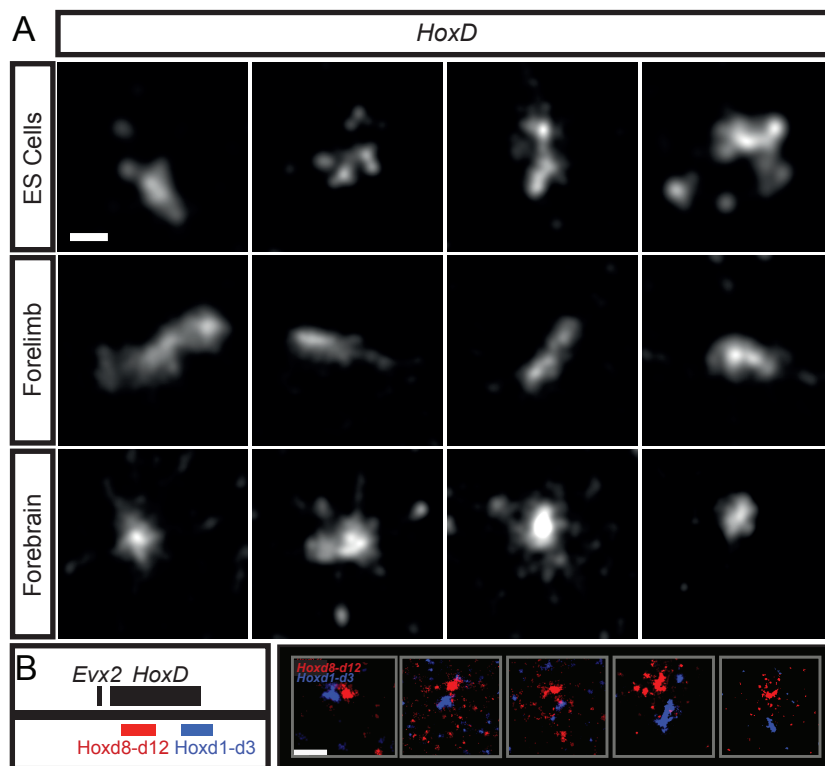


Figure S2: Diversity of *HoxD* morphologies in different cell types. The images illustrate the variability in the shape of objects observed after DNA-FISH using a full *HoxD* cluster probe, followed by STORM imaging. Variability is particularly obvious when looking at ES cells, even though compact structures are not scored (upper panels). In forelimb cells (middle panels), elongated structures are preponderant whereas forebrain cells (lower panels) generally display a much more compact signal. Scale bar: 200nm. (B) Two-colors DNA-FISH showing various configurations of either compacted (left) or de-compacted (right) part of the *HoxD* cluster (scheme in the left panel).

Supplemental Figure S3

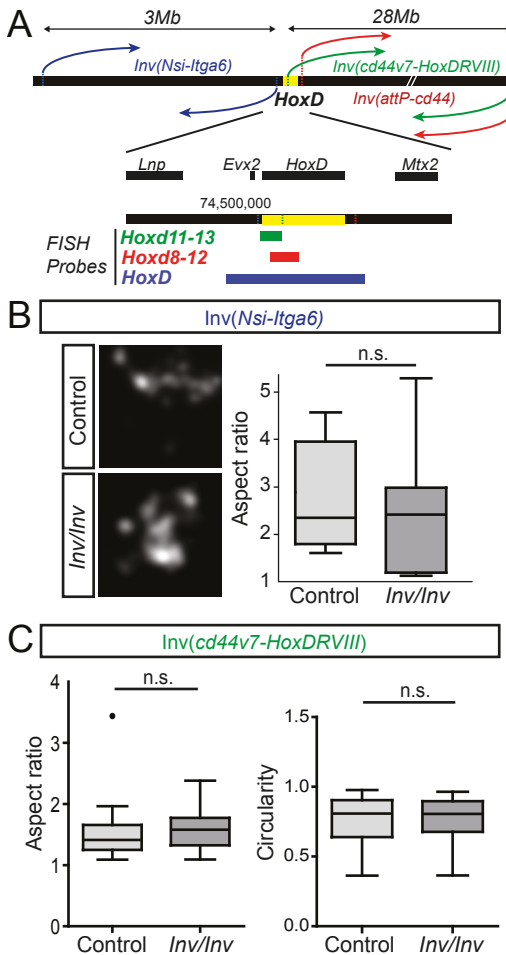


Figure S3: Impact of the two flanking TADs upon condensation of the *HoxD* cluster. (A) Schematics of the three large targeted inversions used in this work as well as of the positions of the BAC and fosmid clones used to monitor elongation (below). The *Inv(Nsi-Itga6)* separates the *HoxD* cluster from its centromeric TAD, whereas the *Inv(attP-cd44)* separates the cluster from its telomeric TAD. The *Inv(cd44v7-HoxDRVIII)* splits the *HoxD* cluster into two small clusters of genes (Spitz et al., 2005). (B) STORM-resolved images obtained with the BAC clone covering the *HoxD* cluster in E12.5 distal forelimbs showed similar de-compacted aspects for both control and inverted alleles in the 3Mb large centromeric (*Inv(Nsi-Itga6)*) inversion. (C) Both aspect ratio and circularity index also remained unchanged for the signals obtained with the *Hoxd11* to *Hoxd13* probe when using the 28Mb large *Inv(cd44v7-HoxDRVIII)* telomeric inversion in E10.5 posterior trunk cells. n.s.: not significant when using Mann-Whitney U test.

Supplemental Figure S4

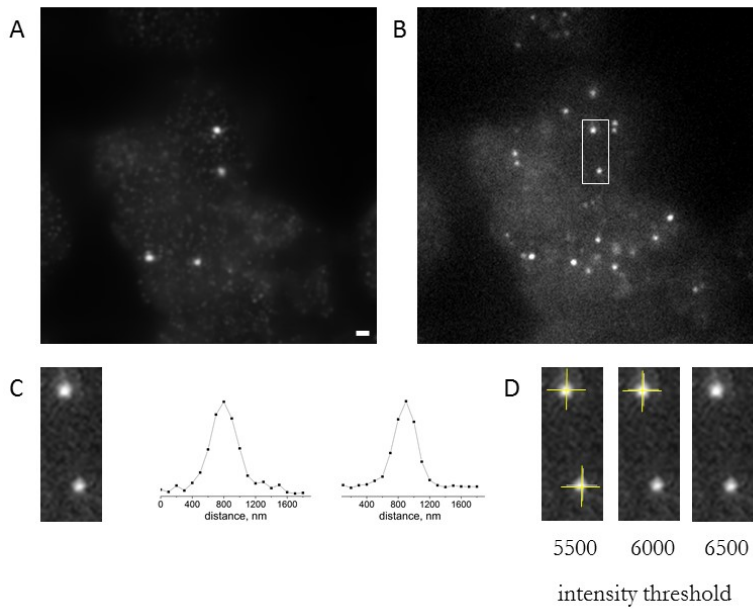


Figure S4: Single molecule peak detection. (A) Standard deviation image of forebrain tissue labeled with *HoxD* cluster probe; bright spots correspond to *HoxD* clusters (scale bar 1 μ m). (B) Single STORM imaging frame. (C) Fluorescent image of two typical single molecules and their fluorescence intensity profiles. (D) Threshold was chosen individually for each image by checking that most of single molecules are detected by software (yellow cross indicates that molecule is detected).

Supplemental Figure S5

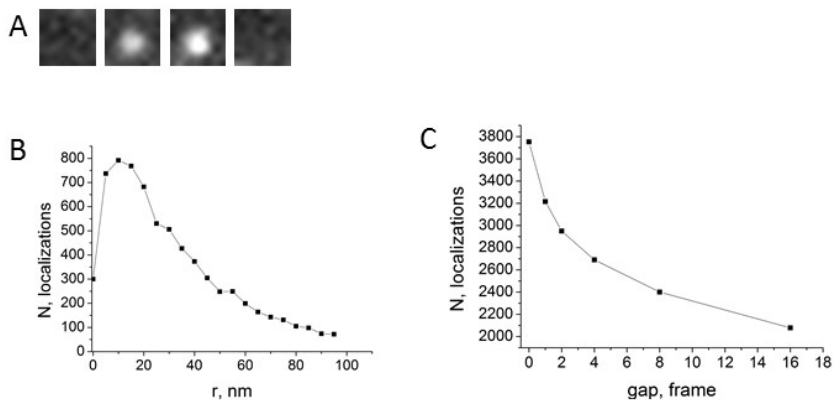


Figure S5: Grouping procedure details. (A) Some molecules are fluorescent for several frames and therefore a grouping correction is needed. (B) Distribution of distances between subsequent localizations of grouped molecules. We note that by using a grouping radius of 100 nm we obtain a non-truncated distribution of step sizes between frames with a mean value far below the maximum search radius, which validates our choice. (C) Number of molecules (after grouping) as a function of grouping gap decays with time but does not plateau. This makes it difficult to find an optimum grouping gap. On one hand it is desirable to introduce at least a gap of one frame in grouping to account for molecules that have borderline intensity and may be

not detected in some frames. On the other hand this gap should not be too long as it can lead to false connection of different molecules. Based on these considerations we picked grouping gap of one frame. As it is stated in the methods, we systematically checked manually that grouping was performed properly.

Supplemental Figure S6

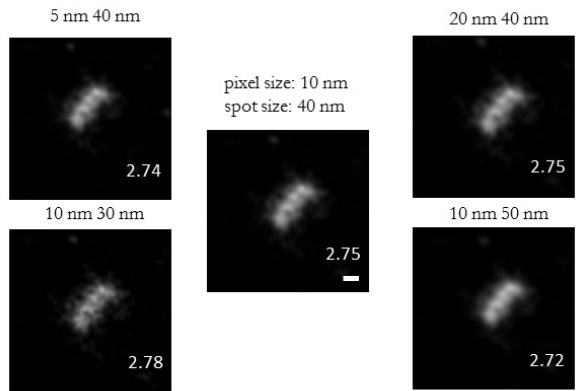


Figure S6: Different rendering parameters do not affect geometrical parameters of a cluster. STORM image of a *HoxD* cluster rendered with different pixel size and different spot size for a single molecule (scale bar 100nm); calculated aspect ratio presented for each rendering condition.

Supplemental Figure S7

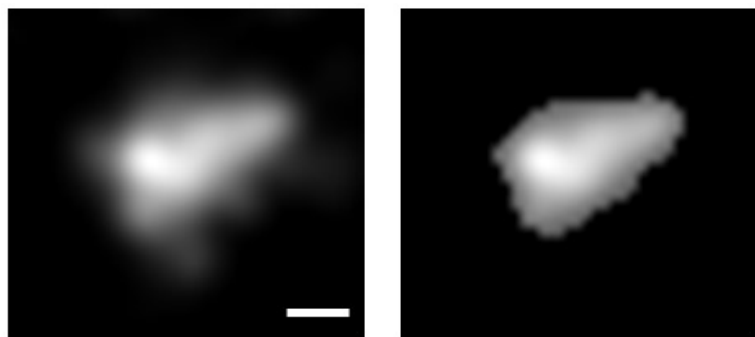


Figure S7: Results of Otsu's algorithm based thresholding. Original image of a *HoxD* cluster (left) and thresholded image (right) (scale bar 100nm).

Supplemental Figure S8

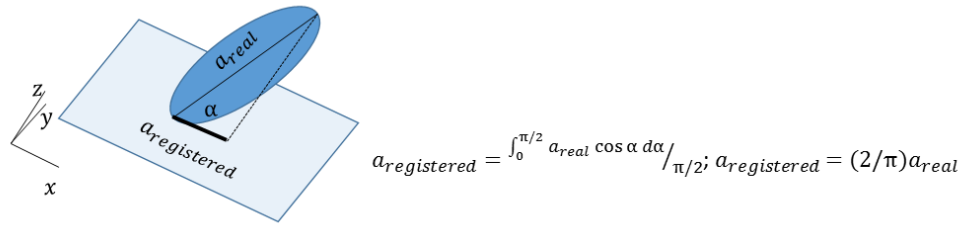


Figure S8: Measured elongation is an underestimation of real elongation. Here, a spheroid with major axis a_{real} and two other axes ($b_{real} = c_{real}$) is imaged (imaging plane XY) as an ellipse with major axis $a_{registered}$ (in this configuration $b_{registered} = b_{real}$) so that the average true 3D elongation ($\pi/2$) ~1.57 larger than the average measured 2D elongation.

Table S1. List of BAC and fosmid clones used for DNA-FISH in the present study. Genomic coordinates are given for mm9.

| | Position | Clone name | Chr | Size | Coordinates (mm9) |
|---------|--------------------------|----------------|-----|---------|-------------------|
| BACs | centro/5' of <i>HoxD</i> | RP23-146O7 | 2 | 207'597 | 73659605 73867202 |
| | centro/5' of <i>HoxD</i> | RP23-427C9 | 2 | 179'151 | 73870783 74049934 |
| | centro/5' of <i>HoxD</i> | RP24-222J8 | 2 | 280'150 | 74050005 74330155 |
| | <i>HoxD</i> | RP24-448E5 | 2 | 158'956 | 74473342 74632298 |
| | telomeric (control) | RPCI-23-374G8 | 2 | 175'293 | 74622622 74797915 |
| | telo/3' of <i>HoxD</i> | RPCI-23-190O13 | 2 | 196'611 | 74552767 74749378 |
| | telo/3' of <i>HoxD</i> | CH29-519G12 | 2 | 225'692 | 74731898 74957590 |
| | telo/3' of <i>HoxD</i> | CH29-617N10 | 2 | 209'323 | 74969620 75178943 |
| | telo/3' of <i>HoxD</i> | CH29-6K11 | 2 | 265'798 | 75192108 75457906 |
| Fosmids | <i>Evx2-Hoxd13</i> | WI1-469P2 | 2 | 38'845 | 74474157 74513002 |
| | <i>Hoxd11-d13</i> | WI1-99N14 | 2 | 29'683 | 74494115 74523798 |
| | <i>Hoxd8-d12</i> | WI1-2777G14 | 2 | 38'891 | 74511607 74550498 |
| | <i>Hoxd3-d4</i> | WI1-2467J14 | 2 | 34'895 | 74550235 74585130 |
| | <i>Hoxd1-d3</i> | WI1-121N10 | 2 | 38'454 | 74566984 74605438 |

Table S2. Statistical significance between the different conditions of interprobe distances presented in Figure 1J. The asterisk * denotes $p < 0.05$, ** for $p < 0.01$ and *** when $p < 0.001$.

| Dunn's Multiple Comparison Test | Difference in rank sum | Significant? $P < 0.05$? | Summary |
|---|------------------------|---------------------------|---------|
| <i>Hoxd8/12-Hoxd13 vs Hoxd3/4-Hoxd13</i> | -134.5 | Yes | *** |
| <i>Hoxd8/12-Hoxd13 vs Hoxd1/3-Hoxd13</i> | -326.9 | Yes | *** |
| <i>Hoxd8/12-Hoxd13 vs Hoxd3/4-Hoxd8/12</i> | -77.36 | Yes | ** |
| <i>Hoxd8/12-Hoxd13 vs Hoxd1/3-Hoxd8/12</i> | -318.9 | Yes | *** |
| <i>Hoxd3/4-Hoxd13 vs Hoxd1/3-Hoxd13</i> | -192.4 | Yes | *** |
| <i>Hoxd3/4-Hoxd13 vs Hoxd3/4-Hoxd8/12</i> | 57.16 | No | ns |
| <i>Hoxd3/4-Hoxd13 vs Hoxd1/3-Hoxd8/12</i> | -184.4 | Yes | *** |
| <i>Hoxd1/3-Hoxd13 vs Hoxd3/4-Hoxd8/12</i> | 249.5 | Yes | *** |
| <i>Hoxd1/3-Hoxd13 vs Hoxd1/3-Hoxd8/12</i> | 7.938 | No | ns |
| <i>Hoxd3/4-Hoxd8/12 vs Hoxd1/3-Hoxd8/12</i> | -241.6 | Yes | *** |

Table S3. Combinations of fluorophores used for 3D DNA-FISH shown in Fig. 1H-K

| Probe | fluor. | Probe | fluor. |
|---------------|-----------|---------------|-----------|
| <i>Hoxd11</i> | Alexa 568 | <i>Hoxd13</i> | Alexa 647 |
| <i>Hoxd13</i> | Alexa 568 | <i>Hoxd3</i> | Alexa 647 |
| <i>Hoxd1</i> | Alexa 647 | <i>Hoxd13</i> | Alexa 568 |
| <i>Hoxd3</i> | Alexa 568 | <i>Hoxd11</i> | Alexa 647 |
| <i>Hoxd1</i> | Alexa 647 | <i>Hoxd11</i> | Alexa 568 |